PAPER

Atomic insights into the oxygen incorporation in atomic layer deposited conductive nitrides and its mitigation by energetic ions†

Saurabh Karwal,*‡[a] Bora Karasulu, [ID] *‡[b] Harm C.M. Knoops,[a,c] Vincent Vandalon,[a] Wilhelmus M.M. Kessels [ID] [a] and Mariadriana Creatore [ID] *[a]

Oxygen is often detected as impurity in metal and metal nitride films prepared by atomic layer deposition (ALD) and its presence has profound and adverse effects on the material properties. In this work, we present the case study of HfN_x films prepared by plasma-assisted ALD by alternating exposures of CpHf $(NMe_2)_3$ and H_2 plasma. First, we identify the primary source of O contamination in the film. Specifically, we find that the extent of O incorporation in HfN_x films is determined by the flux of background H_2O/O_2 residual gases reaching the HfN_x surface during the ALD process and leads to the formation of Hf–O bonds. Then, we report on the decrease in the concentration of Hf–O bonds in the film upon application of an external radiofrequency (rf) substrate bias during the H_2 plasma step. The experimental work is accompanied by first principles calculations to gain insights into the O incorporation and its mitigation upon the impingement of energetic ions on the surface. Specifically, we find that the dissociative binding of H_2O on a bare HfN surface is highly favored, resulting in surface Hf–OH groups and concomitant increase in the oxidation state of Hf. We also show that energetic cations (H^+, H_2^+ and H_3^+) lead to the dissociation of surface Hf–OH bonds, H_2O formation, and its subsequent desorption from the surface. The latter is followed by reduction of the Hf oxidation state, presumably by H• radicals. The atomic-level understanding obtained in this work on O incorporation and its abstraction are expected to be crucial to prevent O impurities in the HfN_x films and contribute to the fabrication of other technologically relevant low resistivity ALD-grown transition metal nitride films.

Introduction

Atomic layer deposition (ALD) has emerged as the method of choice for the synthesis of ultra-thin, uniform and highly conformal layers, required in the fabrication of advanced nanoscale device architectures.[1–4] At the same time, control over the film properties in terms of chemical composition and microstructure is highly important. When specifically referring to the metal and metal nitride films prepared by ALD, oxygen is often detected as impurity.[5–7] An interesting class of materials to evaluate the effect of oxygen contamination is one of conductive transition metal nitride (TMN) films, such as TiN_x, TaN_x, MoN_x, HfN_x. In fact, oxygen contamination can be directly related to the decrease in electrical conductivity, as illustrated in the literature overview for various TMN films (ESI section A, Table S1†).[8–28] In particular, Musschoot *et al.* and Langereis *et al.* reported on the inevitable oxygen incorporation in TiN_x and TaN_x films and suggested residual H_2O in the reactor background and/or process gases as potential sources of oxygen contamination in the films.[21,22] Furthermore, Krylov *et al.* demonstrated that also the erosion of the quartz tube can lead to oxygen impurities whereas Rayner *et al.* did an extensive and systematic study of the possible origins of the impurities.[20,24] However, these observations have not been followed by in-depth analysis of the surface reactivity of TMN films towards H_2O/O_2.

Recently, we have reported on the growth of the conductive phase of hafnium nitride (δ-HfN) by adopting CpHf(NMe_2)_3 as Hf(IV) precursor and H_2 plasma as co-reactant.[13,14] We observed that the HfN_x films contained 20 at.% oxygen.[14] Furthermore, due to the formation of Hf–O bonds, a low Hf(III) oxidation state fraction of 0.65 was detected, contributing to a

[a]*Department of Applied Physics, University of Technology Eindhoven, 5600MB, P.O. Box 513, Eindhoven, Netherlands. E-mail: s.karwal@tue.nl, m.creatore@tue.nl*
[b]*Department of Chemistry, University of Warwick, Gibbet Hill Road, Coventry, CV4 7AL, UK. E-mail: bora.karasulu@warwick.ac.uk*
[c]*Oxford Instruments Plasma Technology, North End, Bristol, BS49 4AP, UK*

rather high film resistivity of 0.9 Ω cm.[14] Moreover, we have also reported a decrease in the film resistivity by two orders of magnitude down to 3.3×10^{-3} Ω cm upon the application of an external radiofrequency (rf) substrate bias during the H_2 plasma step with a time-averaged potential value (V_{bias}) of −130 V.[13] This resulted from a decrease in oxygen content to below 2.0 at.% and a correlated increase in the Hf(III) fraction up to 0.82.[13] These results suggest a correlation between the decrease in oxygen content in the films and the increase in the average energy of incident ions (E_{ion}). However, the mechanism of the suppression of oxygen content enabled by energetic ions was not explored.

In this work, we first elucidate the primary source of oxygen incorporation in the film and study the dependence of oxygen content as a function of the total ALD cycle time. We find a gradual increase in the oxygen content when the ALD cycle time is increased. Subsequently, we demonstrate a gradual decrease in the density of Hf–O bonds in the HfN_x films with an increase in E_{ion}, enabled by the application of external rf substrate bias. By means of first-principles density functional theory (DFT) calculations, we provide an atomistic insight into the kinetics of chemisorption of gaseous H_2O/O_2 on the pristine HfN surface that leads to formation of surface Hf–OH groups. Subsequently, we show that energetic cations in the H_2 plasma trigger the dissociation of surface Hf–OH bonds and lead to H_2O formation, followed by its desorption. In addition, we hypothesize that the H• radicals in the H_2 plasma reduce Hf(IV) to Hf(III) subsequent to H_2O desorption, in-line with our previous report.[13] The atomic-level understanding of the oxygen incorporation and the underlying mechanism of its removal provided here is expected to be key in devising efficient approaches for preventing oxygen impurities in the ALD-grown metal nitride and metal films.

Methods

The plasma-assisted ALD process of HfN_x films was carried out in an Oxford Instruments FlexAL ALD reactor that is equipped with an inductively coupled remote plasma (ICP) source with an alumina dielectric tube.[6,29] A base pressure of 10^{-6} Torr was achieved in the reactor chamber using a turbomolecular pump before every deposition. Briefly, the metal–organic Hf(IV) precursor $CpHf(NMe_2)_3$ was used and an H_2 plasma served as the reducing co-reactant. The details of the recipe can be found elsewhere.[14] An ALD cycle under saturation conditions comprised of a $CpHf(NMe_2)_3$ pulse of 4 s and H_2 plasma exposure of 10 s, while keeping the purge steps of 2 s after every half cycle (ESI section B, Fig. S1†). An external rf substrate bias was applied during the H_2 plasma exposure. As a result of bias application, a time-averaged negative potential with respect to ground develops at the substrate (V_{bias}).[13,30] The magnitude of the developed V_{bias} was tuned by varying the applied rf power transmitted to the substrate holder as previously reported.[13] Furthermore, as a result of negative substrate potential, the average energy of exclusively the cationic

species in the plasma is enhanced by accelerating them towards the HfN surface. The substrate holder was heated to 450 °C which corresponds to an actual substrate temperature of 340 °C.[13] Si(100) with a diameter of 100 mm and with 450 nm SiO_2 atop was used as the substrate on which ∼30 nm–40 nm HfN_x films were deposited. Using thick SiO_2 (insulating and transparent film) enables an accurate measurement of resistivity and optical constants of the HfN_x films.

X-ray photoelectron spectroscopy (XPS) measurements were performed using a Thermoscientific K-Alpha KA1066 system equipped with a monochromatic Al Kα ($h\nu$ = 1486.6 eV) source in order to study the chemical bonds and the oxidation states of the elements present in the film. XPS measurements were carried out by first sputtering the HfN_x film for 500 s (8 nm–10 nm) by Ar^+ ions with low energy of 200 eV. This was done in order to eliminate the contribution of surface impurities from the first few layers of HfN_x film and to ensure the measurement of chemical composition of the bulk HfN_x film precisely. Rutherford backscattering spectrometry (RBS) was performed using 1900 keV $^4He^+$ ions (Detect99) with two detectors at scattering angles of 170° and 150° in order to study the chemical composition of the HfN_x layers.

All electronic structure calculations were done using the projector augmented wavefunction (PAW)[31,32] as implemented in Vienna *Ab Initio* Simulation Package (VASP, v.5.3.5).[33–36] Generalized gradient approximation (GGA) to DFT[37,38] was used jointly with the Perdew–Burke–Ernzerhof (PBE) exchange correlation functional.[39,40] DFT(PBE)-D3 corrections with Becke-Jonson damping[41] were employed to account for van der Waals interactions on an empirical basis (see ESI section C1† for further computational details).

Results

Our initial experiments were focused on the investigation of the primary source of oxygen incorporation in the HfN_x films. This was probed by adding a pump-down step following the H_2 plasma exposure in order to bring the reactor down to the vacuum base pressure (ESI section B, Fig. S1†). The duration of the pump-down step was varied from 0 s to 80 s, thereby increasing the total ALD cycle time from 20 s to 100 s. This additional pump-down step exposed the HfN_x surface only to the residual gases in reactor background. Fig. 1a shows the O 1s XPS spectra of the HfN_x films as a function of total ALD cycle time. A gradual increase in O 1s peak associated to Hf–O bonds is observed when increasing the total ALD cycle time, leading to a steady decrease in Hf(III) fraction from 0.65 ± 0.02 to 0.47 ± 0.02. This result suggests that oxygen content in the HfN_x layers is determined by the total flux of residual H_2O/O_2 gases in the reactor background reaching the HfN_x surface. In every ALD cycle, this pristine HfN_x surface is exposed to the vacuum conditions for a relatively long time, making it susceptible to oxidation even at a vacuum base pressure of 10^{-6} Torr. Relevantly, Kroll *et al.* showed that the oxygen incorporation
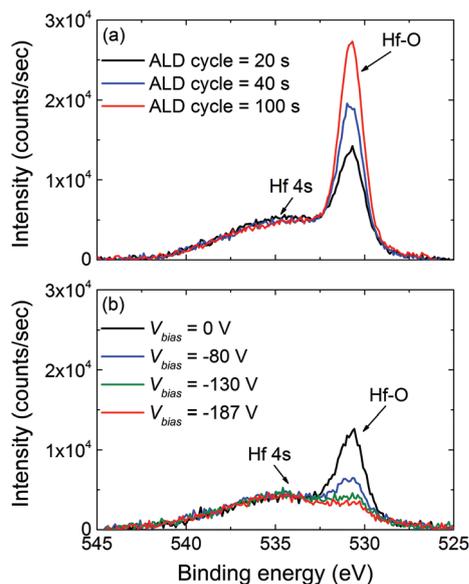
Fig. 1 O 1s XPS spectra for the (a) HfN$_x$ films prepared with grounded substrate (V_{bias} = 0 V) showing an increase in the O 1s peak associated to Hf−O bonds as a function of ALD cycle time. The difference in ALD cycle time is due to an extension of the pump-down time of the reactor. (b) HfN$_x$ films grown at various values of V_{bias} illustrating a steady decrease in the O 1s peak associated to Hf−O bonds from 20.1 at.% to <2.0 at.% upon increasing the V_{bias} from 0 V to −130 V and above. The corresponding film resistivity decreased from 0.9 Ω cm at V_{bias} = 0 V to 9.7 × 10^{-3} Ω cm at V_{bias} = −80 V and to 3.3 × 10^{-3} Ω cm at V_{bias} = −130 V.[13]

in a-Si:H films prepared by plasma-enhanced CVD was enhanced at lower deposition rates.[19] The reactor outgassing, i.e. release of residual gases, was identified as one of the primary reason for oxygen contamination.[19] The lower the deposition rate of a-Si:H films, the more important is the flux of outgassed residual gases. In our case, in order to illustrate that even very low background pressures can lead to significant oxygen incorporation in the film, the flux of H$_2$O molecules impinging on the HfN$_x$ surface was calculated using the Hertz-Knudsen equation (see ESI section B†). Using these calculations, an oxygen content of 39% is deduced assuming an H$_2$O partial pressure of 10^{-8} Torr and a sticking probability of 1 for ALD cycle time of 20 s. This calculation reveals that a significant O content in the film can result even from a very low background H$_2$O partial pressure.

The effect of application of external rf substrate bias on the oxygen content in the HfN$_x$ films was subsequently investigated. The HfN$_x$ films were prepared using a H$_2$ plasma exposure of 10 s (no pump-down step) and the magnitude of V_{bias} was gradually increased from 0 V to −187 V during the H$_2$ plasma half cycle. Fig. 1b shows the O 1s XPS spectra as a function of the value of V_{bias}. Interestingly, the O 1s peak associated to Hf−O bonds significantly decreased upon increasing the V_{bias} from 0 V to −80 V, suggesting a decrease in the density of Hf−O bonds. Moreover, an increase in the V_{bias} to

−130 V or higher led to a saturation in decrease of Hf−O peak intensity, yielding an oxygen content below 2.0 at.% as determined by RBS.[13] Energetic ions may lead to the physical sputtering of oxygen. In the case of sputtering, a decrease in the areal density of nitrogen atoms is also expected to occur in parallel. In contrast, we reported an increase in the areal density of nitrogen atoms per cycle from 0.71 ± 0.03 atoms per nm^2 at V_{bias} = 0 V to 1.53 ± 0.08 atoms per nm^2 at V_{bias} = −130 V.[13] This cannot be simply explained by sputtering. Therefore, a preferential abstraction of oxygen (and containing groups) is expected as a result of the impingement of energetic ions on the surface of growing film. The seminal works of Sigmund and Steinbrüchel show that ca. 10 times higher ion energy values than the bond energy value is required in order to dissociate molecular bonds, due to the inefficient transfer of the ion energy to the film surface.[42,43] Following this, Kanarik et al. recently reported on the requirement of Ar$^+$ ions with an E_{ion} of ca. 50 eV in order to enable the dissociation of Si–Si bonds with a bond energy of 2.3 eV in order to facilitate the atomic layer etching of Si.[44,45] In our case, assuming a similar energy transfer factor, an E_{ion} of ~90–100 eV seems adequate to dissociate the surface Hf−O bonds with a high bond energy of ~5.4 eV, as computed using DFT calculation as will be shown later.

In order to gain insights into the oxygen incorporation in the HfN$_x$ films and its mitigation upon delivery of energetic ions to the surface, detailed DFT calculations were carried out. To this end, the dissociative binding of H$_2$O and O$_2$ on a bare HfN surface was simulated. Three δ-HfN models were generated for DFT simulations: one HfN(200) surface with equivalent N- and Hf- termination and two HfN(111) surface with either Hf- or N- termination (see ESI section C2, Fig. S2† for the discussion on HfN surface termination). The DFT calculations indicate that the surface energies for HfN(200) and HfN(111) surfaces are 10 eV nm^{-2} and 15 eV nm^{-2}, respectively. This result suggests that HfN(200) surface is likely the predominant orientation.[13] This is in-line with our experimental observations on the growth of polycrystalline δ-HfN$_x$ films, with the co-existence of HfN(200) and HfN(111) orientations at V_{bias} = 0 V and V_{bias} = −130 V.[13] For brevity, we discuss here the results for the case of HfN(200) surface, whereas similar results for Hf(111) surface can be found in the ESI (section D2†).
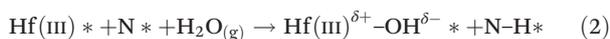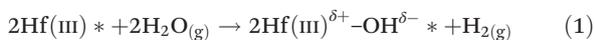
Ab initio molecular dynamics (AIMD) simulations were performed to generate canonical (NVT) ensembles at 1000 K in vacuum environment, using 1 fs time step for a set of at least 3.0 ps trajectories. The model system used for bare HfN(200) surface contained 32 Hf and 32 N atoms on the topmost surface (ESI, section C2†). A total of 16 H$_2$O molecules were placed atop the HfN(200) surface, providing a surface coverage ratio of one H$_2$O molecule per two surface Hf sites (i.e. Hf:O = 2:1). MD simulations suggest that following a dissociative binding process, H$_2$O molecules bind exclusively to Hf atoms, leading to the formation of Hf−OH bonds (Fig. 2), supporting the XPS results of Fig. 1a. Similar results were obtained for Hf(111) surface (see ESI section D2, Fig. S3† and the related discussion).
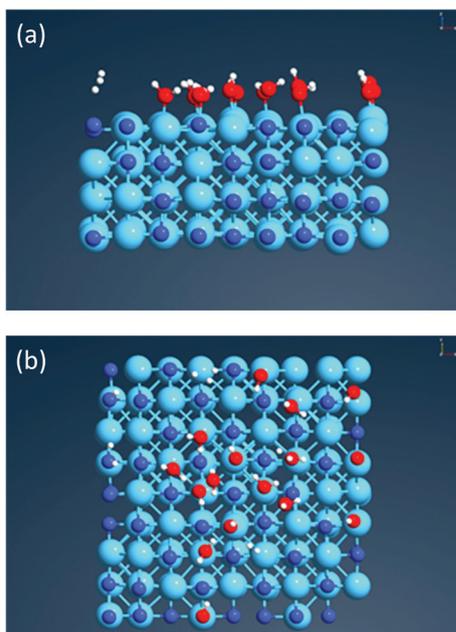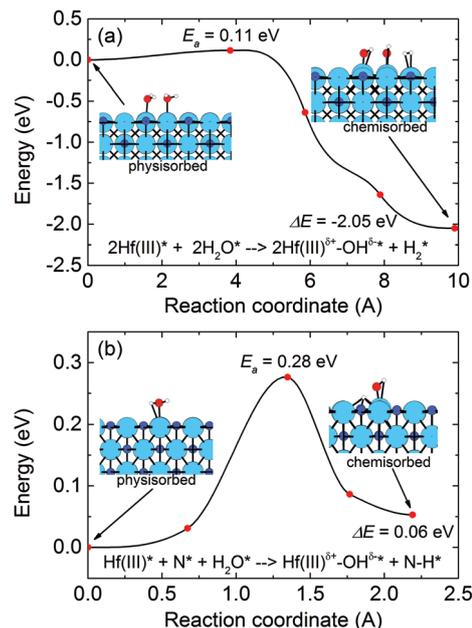
Fig. 2 (a) Side-view and (b) top-view snapshot from the AIMD simulation of the thermal hydroxylation of bare HfN(200) surface. A total of 16 H_2O molecules were added to provide a coverage ratio of Hf : O = 2 : 1. Color code: cyan: Hf; blue: N; red: O; white: H.

Fig. 3 DFT/PBE-D3 level minimum-energy paths (MEPs) for the dissociative binding of H_2O molecule(s) on the bare HfN(200) surface following the pathways as described in (a) eqn (1) and (b) eqn (2). The physisorption energies (with respect to the isolated HfN surface and H_2O molecule) are −0.88 and −0.80 eV per H_2O adsorbate, respectively, indicating a high surface sticking probability. Color code: cyan: Hf; blue: N; red: O; white: H.

Furthermore, the dissociative binding of H_2O molecules could proceed *via* two routes. The first involves the combination of two H_2O molecules to yield a H_2 molecule, with the two –OH groups easily binding on two Hf(III) sites (eqn (1)). The second route involves the binding of one –OH group at the Hf-site, whereas the additional H is transferred to the neighbouring N-site (eqn (2)).

$$2Hf(III) * + 2H_2O_{(g)} \rightarrow 2Hf(III)^{\delta+}\text{–}OH^{\delta-} * + H_{2(g)} \quad (1)$$

$$Hf(III) * + N * + H_2O_{(g)} \rightarrow Hf(III)^{\delta+}\text{–}OH^{\delta-} * + N\text{–}H* \quad (2)$$

*denotes surface species, whereas partial charges are represented by $\delta+$, $\delta-$. Partial charges are only present to the surface as Hf(III)–N bonds are present in the bulk.

AIMD simulations suggest route 1 is most likely to occur, as concluded from the released H_2 molecules and the absence of amine groups (N–H) (see Fig. 2 and ESI section D2, Fig. S3† for snapshots from the relevant MD trajectories). For a more quantitative comparison, the climbing-image nudged elastic band (CI-NEB) method was utilized for concerted binding of two H_2O molecules on a pristine HfN(200) surface following each pathway. Fig. 3 shows the resulting minimum energy paths (MEPs) revealing that unlike the second pathway (eqn (2)), which has a high activation energy (E_a = 0.28 eV), the first one (eqn (1)) is both kinetically and thermodynamically highly feasible (E_a = 0.11 eV and ΔE = −2.05 eV), in-line with the above AIMD results. Furthermore, it should be noted that by assuming the pre-exponential factors in the Arrhenius equation to be similar in magnitude for the two reactions, at

25 °C the difference in kinetic barrier translates into a rate constant 750 times higher for route 1 than route 2.

Based on the AIMD and NEB results, it can be concluded that the binding of H_2O on a pristine HfN surface is expected to proceed *via* route 1, leading to surface Hf–OH groups. The overall reaction for hydroxylation of bare HfN surface can thus be written as in eqn (1), whereas the corresponding hypothesized redox half reactions are discussed in the ESI (section D2, eqn (S3)–(S7)†).

Furthermore, the low E_a agrees well with the easy incorporation of oxygen in the HfN_x films prepared by plasma-assisted ALD with the grounded electrode as discussed earlier. It is worth mentioning that the reverse reaction (*i.e.* associative desorption of H_2O) is energetically unfeasible, involving high energy barriers and high endothermicity. The latter conclusion falls in line with the high bond energy of ~5.4 eV for surface Hf–OH bonds, as computed using DFT calculations (see section D2, eqn (S8)† and the related discussion), rendering surface –OH groups thermodynamically stable.

Related to this point, DFT calculations predict a strong initial physisorption of the H_2O molecules (−0.88 and −0.80 eV per H_2O molecule), which implies a low desorption rate as compared to the dissociative binding of H_2O on the surface with low activation energies (see above). Taken together a high surface sticking probability is predicted, whereas the entropic contributions play a minor role in the sticking probability due to the small size of the adsorbate.

Alongside the background H_2O, the dissociative binding of gaseous O_2 on HfN surface was also investigated (see ESI section D3 for detailed discussion, Fig. S4†). The dissociative binding of O_2 on HfN surface is found to be kinetically hindered ($E_a = 0.25$ eV) when compared to chemisorption of H_2O.

The effect of energetic ions on surface functionalization was investigated next. First, the binding energies of distinct species in a H_2 plasma towards surface –OH group was determined using static *ab initio* DFT calculations. Here, the plasma species have not been assigned any initial velocity (*i.e.* the species are without kinetic energy) and only the chemical affinity of different plasma species towards the surface –OH groups is probed. For simplicity, the HfN(200) surface was assumed to be fully hydroxylated (with Hf/O = 1 : 1), along with a fully oxygenated one (with Hf/O = 2 : 1) for comparison purposes (see ESI section E1, Fig. S5† for further discussion). Bader charge analysis[46,47] reveals that the binding of 32 –OH groups leads to an increase in the total charge of HfN slab by *ca.* 16*e*, in-line with the partial oxidation of Hf(III) to Hf(III)$^{\delta+}$ (see note[48] for a detailed discussion).

Based upon the experimental work of Sode *et al.*,[49] a H_2 plasma discharge is expected to contain H^-, H^+, H_2^+ and H_3^+ ions and $H^{\bullet}$ radicals species. Table 1 summarizes the computed binding energies of all the possible H_2 plasma species with the surface –OH groups at the PBE-D3 level. Furthermore, the corresponding reaction products as a result of their binding with surface –OH groups are also reported. The products are determined as a part of structure optimization procedure. Furthermore, since the plasma species were not given kinetic energy, the reaction products formed remain chemisorbed on the surface in their intermediate forms (for example, H^+ ions lead to formation of surface Hf–$[H_2O]^+$ bonds).

It can be concluded that the cationic species (H^+, H_2^+ and H_3^+) show the highest affinity for the surface –OH groups. Furthermore, the cationic species are predicted to form H_2O as a product upon reacting with surface –OH groups. In contrast, the anionic (H^-, H_2^- and H_3^-) and neutral (H, H_2 and H_3) species are (energetically) reluctant to react with the surface –OH groups. The anionic and neutral species in the H_2 plasma

were found to yield volatile H_2 products, leaving the surface –OH groups intact (see ESI section E2† for the results on fully oxygenated HfN surface).

Based on the energetics results, a set of redox half reactions that likely underlie the binding of H^+ ions on Hf–OH surface groups are proposed and can be found in the ESI (section E3, eqn (S10)–(S14)†). Moreover, we hypothesize that following the liberation of H_2O from the HfN surface, $H^{\bullet}$ radicals in the plasma near the surface restore the pristine HfN surface *via* reduction of Hf(IV) to Hf(III) in a concerted reaction pathway (eqn (S12) and (S13)†), in-line with the previously reported XPS results.[14] This hypothesis is also based on the application of H_2 plasma to reduce the Pt(IV) and Ta(V) in the precursor to synthesize metallic Pt(0) and Ta(III)N films with ALD.[50,51]

Based on the experimental observations of the mitigation of oxygen incorporation due to energetic ions, a set of AIMD simulations were designed to probe this effect at molecular level. As aforementioned, the average energy (E_{ion}) of the highly-reactive cationic species (H^+, H_2^+ and H_3^+) in our experimental work is controlled by the application of external rf substrate bias.[13,30] In these simulations, the fully hydroxylated HfN surface model (as previously introduced, Fig. S5†) was again assumed. In addition, 16 hydrogen cations (H^+) were placed randomly 4.5 Å above the hydroxylated HfN surface in three separate tries (which differ in terms of initial H^+ positions), and all ions were assigned with the same initial velocities directed towards the surface. A sample simulation model is visualized in Fig. 4a. Two cases with ion velocities of
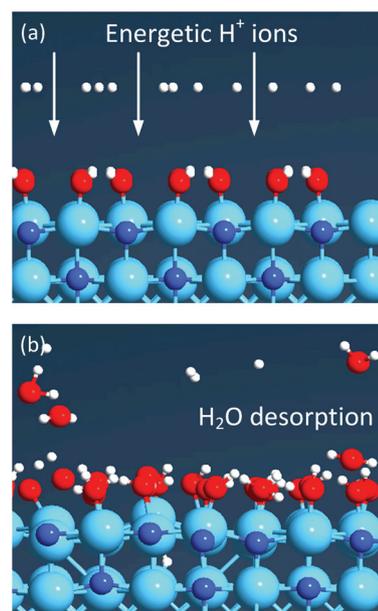

Fig. 4 *Ab initio* molecular dynamics (AIMD) simulation snapshots illustrating the desorption of H_2O resulting from the impingement of energetic H^+ ions with a velocity of 1.75 Å fs^{-1} on a fully hydroxylated HfN (200) surface at (a) $\Delta t = 0.0$ fs and (b) 350.0 fs. Color code: cyan: Hf; blue: N; red: O; white: H. See ESI section E4, Fig. S6† for additional snapshots of the movies and a real-time video file can be found in the ESI.†

Table 1 DFT/PBE-D3 level binding energies (E_b) of various hydrogen-containing plasma species on a hydroxylated HfN surface and the type of volatile product(s) being formed. The most reactive species (*i.e.* cations), their E_b and type of products are given in bold. Only a single adsorbent species is considered for computing the E_b of each adsorbing species

Species	E_b ^{a} [eV]	Reaction product(s)
H^-/H/**H^+**	0.05/−1.81/**−2.25**	H_2/H_2/**H_2O**
H_2^-/H_2/**H_2^+**	1.00/0.06/**−14.71**	—/—/**2H_2O**
H_3^-/H_3/**H_3^+**	2.30/−2.17/**−12.95**	$2H_2$/$2H_2$/**H_2O + H_2**

^{a} Binding energies are computed using $E_b = E_p - E_H - E_s$, where E_p is the product energy, E_H and E_s energies of the isolated hydrogen containing species and isolated hydroxylated HfN surface.
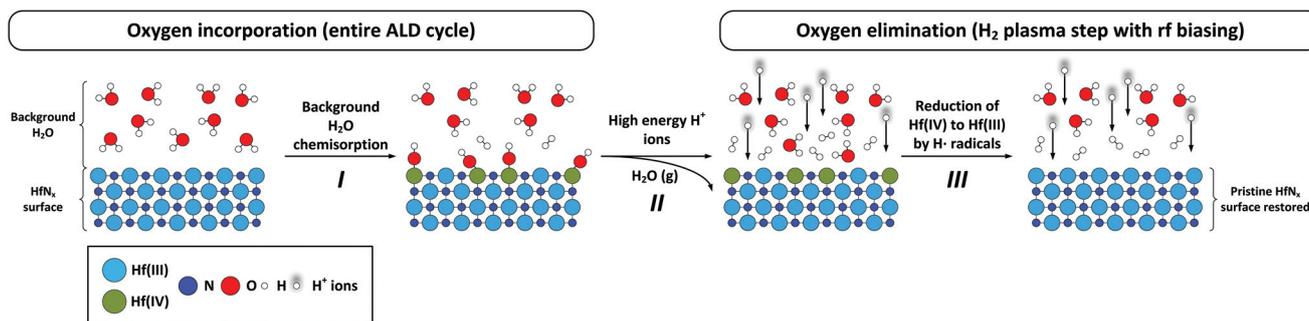
Fig. 5 A schematic summary of the oxygen incorporation and elimination mechanisms proposed in this work. The H_2O chemisorption occurs during the entire ALD cycle and leads to the hydroxylation of HfN surface and the formation of Hf−OH bonds. The liberation of H_2O and subsequent reduction of Hf(IV) to Hf(III) takes place only during the H_2 plasma half cycle, resulting from the impingement of energetic cations. It should be noted that only a part of the entire ALD cycle is depicted.

$\nu_i = 0.76$ Å fs^{-1} and $\nu_i = 1.75$ Å fs^{-1} were assumed in order to roughly model the resulting kinetic energy for the grounded electrode and rf substrate bias conditions (see ESI section E4, Table S5† for a substantiation of these values). The ions with a lower initial velocity did not lead to dissociation of surface Hf–OH bonds. AIMD simulations point at the formation of intermediate surface Hf–[H_2O]$^+$ species, which remains chemisorbed on the surface, and later dissociates to yield again the Hf–OH surface bonds. On the other hand, the ions with a higher initial velocity lead to abstraction of –OH groups from the surface and H_2O liberation was observed within the same time frame (*e.g.* 350 fs simulation) (Fig. 4b). It should also be noted here that the DFT calculations were performed only for the H$^+$ ions to limit the computational efforts, however the H$_2^+$ and H$_3^+$ ions are expected to yield similar results.

So far, we have discussed a one-off ion exposure event (*i.e.* a single layer of ions impacting the surface), while the HfN surface experiences a continuous flux of energetic ions in reality. In an attempt to crudely account for the continuous energetic ion flux, we performed analogous MD simulations with two layers of 16 H$^+$ ions (instead of one) in the simulation model (with 3.5 Å interlayer separation, data not shown). An extra layer of H$^+$ ions with a ν_i value of 1.75 Å/fs indeed led to an increase in the number of removed surface –OH groups as volatile H_2O products with respect to a single layer H$^+$ ions, thus suggesting an enhanced removal of the surface –OH groups upon increasing ion flux (see ESI section E5† for the discussion on surface termination subsequent to the abstraction of all surface –OH groups).

that lead to the oxidation of the HfN$_x$ surface by first principles DFT calculations. In addition, the kinetics of O elimination by energetic ions upon application of external rf substrate bias during the H_2 plasma step is addressed. The corresponding events of H_2O chemisorption on the HfN surface and Hf–O bond dissociation and H_2O formation due to impingement of energetic ions are schematically summarized in Fig. 5.

We show that the O content in the HfN$_x$ layers is determined by the total flux of H_2O/O_2 impinging on the HfN$_x$ surface during the entire ALD cycle. Next, we observed that an increase in the time-averaged substrate potential from 0 V to −130 V leads to a decrease in the density of Hf–O bonds in HfN$_x$ films due to the impingement of energetic ions.

By using DFT calculations, we found that the chemisorption of H_2O on the bare HfN surface is kinetically and thermodynamically highly feasible, creating hydroxyl (Hf–OH) surface groups (**I**, Fig. 5). DFT calculations also revealed that only the cationic species (H$^+$, H$_2^+$, H$_3^+$) present in H_2 plasma are highly reactive towards the surface –OH groups. Moreover, an increase in the energy of incident cations was shown to not only dissociate Hf–OH surface bonds but also lead to H_2O formation and desorption (**II**, Fig. 5). In addition, the H$^{\bullet}$ radicals present in H_2 plasma are hypothesized to reduce Hf(IV) to Hf(III) subsequent to H_2O liberation (**III**, Fig. 5), in line with previously reported increase in Hf(III) fraction. These reactions can be considered as contributing to a so-called atomic layer cleaning (ALC) process.[52]

In perspective, these results shed light on the mechanism of oxygen incorporation and its mitigation for a wide range of ALD processes, where surfaces with high affinity towards oxidation are considered, such as TiN$_x$, HfN$_x$, MoC$_x$, Ta, and enable ALD of low resistivity films with potential application in nano-electronics.[10,53,54]

Conclusions

Suppressing the oxygen contamination is a well-known challenge in the synthesis of conductive metal nitride and metal thin films by ALD, since oxygen limits their electrical conductivity. Here, we present a study on the O incorporation in conductive metal nitrides by using plasma-assisted ALD of HfN$_x$ films as a case study. We investigate the atomic-level processes

Conflicts of interest

All authors have given approval to the final version of the manuscript. There are no conflicts to declare.

Acknowledgements

Notes and references

1 J. W. Elam, J. A. Libera, T. H. Huynh, H. Feng and M. J. Pellin, *J. Phys. Chem. C*, 2010, **114**, 17286–17292.

2 S. Haukka, E.-L. Lakomaa, O. Julha, J. Vilhunen and S. Hornytzkyj, *Langmuir*, 1993, **9**, 3497–3506.

3 E. L. Lakomaa, A. Root and T. Suntola, *Appl. Surf. Sci.*, 1996, **107**, 107–115.

4 J. Keranen, C. Guimon, E. Iiskola, A. Auroux and L. Niinisto, *J. Phys. Chem. B*, 2003, **107**, 10773–10784.

5 D. Eom, S. Y. No, C. S. Hwang and H. J. Kim, *J. Electrochem. Soc.*, 2006, **153**, C229–C234.

6 H. C. M. Knoops, E. M. J. Braeken, K. De Peuter, S. E. Potts, S. Haukka, V. Pore and W. M. M. Kessels, *ACS Appl. Mater. Interfaces*, 2015, **7**, 19857–19862.

7 H. B. R. Lee, W. H. Kim, J. W. Lee, J. M. Kim, K. Heo, I. C. Hwang, Y. Park, S. Hong and H. Kim, *J. Electrochem. Soc.*, 2010, **157**, D10–D15.

8 A. Bertuch, B. D. Keller, N. Ferralis, J. C. Grossman and G. Sundaram, *J. Vac. Sci. Technol., A*, 2017, **35**, 01B141.

9 S. Consiglio, W. Zeng, N. Berliner and E. T. Eisenbraun, *J. Electrochem. Soc.*, 2008, **155**, H196–H201.

10 T. Faraz, H. C. M. Knoops, M. A. Verheijen, C. A. A. van Helvoirt, S. Karwal, A. Sharma, V. Beladiya, A. Szeghalmi, D. M. Hausmann, J. Henri, M. Creatore and W. M. M. Kessels, *ACS Appl. Mater. Interfaces*, 2018, **10**, 13158–13180.

11 S. B. S. Heil, E. Langereis, F. Roozeboom, M. C. M. Van De Sanden and W. M. M. Kessels, *J. Electrochem. Soc.*, 2006, **153**, G956–G965.

12 J. Hinz, A. J. Bauer and L. Frey, *Semicond. Sci. Technol.*, 2010, **25**, 075009.

13 S. Karwal, M. A. Verheijen, B. L. Williams, T. Faraz, W. M. M. Kessels and M. Creatore, *J. Mater. Chem. C*, 2018, **6**, 3917–3926.

14 S. Karwal, B. L. Williams, J. P. Niemelä, M. A. Verheijen, W. M. M. Kessels and M. Creatore, *J. Vac. Sci. Technol., A*, 2017, **35**, 01B129.

15 E. J. Kim and D. H. Kim, *Electrochem. Solid-State Lett.*, 2006, **9**, C123–C125.

16 J. Y. Kim, D. Y. Kim, H. O. Park and H. Jeon, *J. Korean Phys. Soc.*, 2004, **45**, 1639–1643.

17 J. Y. Kim, S. Seo, D. Y. Kim, H. Jeon and Y. Kim, *J. Vac. Sci. Technol., As*, 2004, **22**, 8–12.

18 H. C. M. Knoops, T. Faraz, K. Arts and W. M. M. Kessels, *J. Vac. Sci. Technol., A*, 2019, **37**, 030902.

19 U. Kroll, J. Meier, H. Keppner, A. Shah, S. D. Littlewood, I. E. Kelly and P. Giannoulès, *J. Vac. Sci. Technol., A*, 1995, **13**, 2742–2746.

20 I. Krylov, X. Xu, K. Weinfeld, V. Korchnoy, D. Ritter and M. Eizenberg, *J. Vac. Sci. Technol., A*, 2019, **37**, 010906.

21 E. Langereis, H. C. M. Knoops, A. J. M. MacKus, F. Roozeboom, M. C. M. Van De Sanden and W. M. M. Kessels, *J. Appl. Phys.*, 2007, **102**, 083517.

22 J. Musschoot, Q. Xie, D. Deduytsche, S. Van den Berghe, R. L. Van Meirhaeghe and C. Detavernier, *Microelectron. Eng.*, 2009, **86**, 72–77.

23 G. Rampelberg, K. Devloo-Casier, D. Deduytsche, M. Schaekers, N. Blasco and C. Detavernier, *Appl. Phys. Lett.*, 2013, **102**, 111910.

24 G. B. RaynerJr, N. O'Toole, J. Shallenberger and B. Johs, *J. Vac. Sci. Technol., A*, 2020, **38**, 062408.

25 M. Ritala, M. Leskelä, E. Rauhala and J. Jokinen, *J. Electrochem. Soc.*, 1998, **145**, 2914–2920.

26 C. Seungchan, L. Keunwoo, S. Pungkeun, J. Hyeongtag and K. Yangdo, *Jpn. J. Appl. Phys.*, 2007, **46**, 4085.

27 M. J. Sowa, Y. Yemane, F. B. Prinz and J. Provine, *J. Vac. Sci. Technol., A*, 2016, **34**, 051516.

28 M. J. Sowa, Y. Yemane, J. Zhang, J. C. Palmstrom, L. Ju, N. C. Strandwitz, F. B. Prinz and J. Provine, *J. Vac. Sci. Technol., A*, 2017, **35**, 01B143.

29 H. C. M. Knoops, K. De Peuter and W. M. M. Kessels, *Appl. Phys. Lett.*, 2015, **107**, 014102.

30 H. B. Profijt, M. C. M. Van De Sanden and W. M. M. Kessels, *J. Vac. Sci. Technol., A*, 2013, **31**, 01A106.

31 P. E. Blöchl, *Phys. Rev. B: Condens. Matter Mater. Phys.*, 1994, **50**, 17953–17979.

32 G. Kresse and D. Joubert, *Phys. Rev. B: Condens. Matter Mater. Phys.*, 1999, **59**, 1758–1775.

33 G. Kresse and J. Furthmüller, *Comput. Mater. Sci.*, 1996, **6**, 15–50.

34 G. Kresse and J. Furthmüller, *Phys. Rev. B: Condens. Matter Mater. Phys.*, 1996, **54**, 11169–11186.

35 G. Kresse and J. Hafner, *Phys. Rev. B: Condens. Matter Mater. Phys.*, 1993, **47**, 558–561.

36 G. Kresse and J. Hafner, *Phys. Rev. B: Condens. Matter Mater. Phys.*, 1994, **49**, 14251–14269.

37 P. Hohenberg and W. Kohn, *Phys. Rev.*, 1964, **136**, B864–B871.

38 W. Kohn and L. J. Sham, *Phys. Rev.*, 1965, **140**, A1133–A1138.

39 J. P. Perdew, K. Burke and M. Ernzerhof, *Phys. Rev. Lett.*, 1996, **77**, 3865–3868.

40 J. P. Perdew, K. Burke and M. Ernzerhof, *Phys. Rev. Lett.*, 1997, **78**, 1396–1396.

41 S. Grimme, J. Antony, S. Ehrlich and H. Krieg, *J. Chem. Phys.*, 2010, **132**, 154104.

42 P. Sigmund, *Phys. Rev.*, 1969, **184**, 383–416.

43 C. Steinbrüchel, *Appl. Phys. Lett.*, 1989, **55**, 1960–1962.

44 S. Sakurai and T. Nakayama, *J. Cryst. Growth*, 2002, **237-239**, 212–216.

45 K. J. Kanarik, T. Lill, E. A. Hudson, S. Sriraman, S. Tan, J. Marks, V. Vahedi and R. A. Gottscho, *J. Vac. Sci. Technol., A*, 2015, **33**, 020802.

46 W. Tang, E. Sanville and G. Henkelman, *J. Phys.: Condens. Matter*, 2009, **21**, 084204.

47 R. F. W. Bader, *Atoms in Molecules: A Quantum Theory*, Oxford University Press, New York, 1990.

48 Comparison of the Bader charges of the bare and hydroxylated HfN models reveals that the binding of –OH groups (with a partial charge of *ca.*−0.52*e* per –OH moiety) triggers a charge transfer away from the surface Hf atoms (amounting to *ca.* 0.35*e*).

49 M. Sode, T. Schwarz-Selinger and W. Jacob, *J. Appl. Phys.*, 2013, **114**, 063302.

50 A. J. M. Mackus, D. Garcia-Alonso, H. C. M. Knoops, A. A. Bol and W. M. M. Kessels, *Chem. Mater.*, 2013, **25**, 1769–1774.

51 H. C. M. Knoops, E. Langereis, M. C. M. v. d. Sanden and W. M. M. Kessels, *J. Vac. Sci. Technol., A*, 2012, **30**, 01A101.

52 T. Faraz, F. Roozeboom, H. C. M. Knoops and W. M. M. Kessels, *ECS J. Solid State Sci. Technol.*, 2015, **4**, N5023–N5032.

53 E. Grady, M. Verheijen, T. Faraz, S. Karwal, W. Kessels and A. Bol, arXiv: Applied Physics, 2019.

54 H. Kim and S. M. Rossnagel, *Thin Solid Films*, 2003, **441**, 311–316.